UNIVERSITY OF ROCHESTER

TWO-COLOR NONLOCAL ABERRATION CANCELLATION

June 25, 2022

Stephen Chapman
Supervised by Dr. Robert Boyd and PhD Student Nick Black

Contents

1 ABSTRACT

Applications of entanglement have been sought after for decades. Recently, entangled photons have been used for non-local aberration cancellation. This experiment works to expand the current research by performing aberration cancellation with non-degenerate signal and idler photons. The entangled photons are created through SPDC. Although aberration cancellations wasn't realized in the time allotted, coincidence counts, an important intermediate result, were found.

2 BACKGROUND

2.1 Entanglement

In 1935 Erwin Schödinger wrote a revolutionary paper discussing what he called *verschränkung* or 'entanglement' between two quantum particles. He believed that entanglement is "the characteristic trait of quantum mechanics"[1]. Now, almost a century later, quantum entanglement is still being researched for potentially amazing applications. In this section, the mathematical and conceptual bases of entanglement will be explained. A brief discussion of its importance to this project will follow.

We begin by considering two particles, denoted in Dirac notation by $|1\rangle$ and $|2\rangle$. These particles belong to Hilbert spaces H_A and H_B, respectively. These two particles make up our closed quantum system, and the quantum states of this two particle system are the tensor product of the individual states.

$$\left|\psi_{12}\right\rangle = |1\rangle \otimes |2\rangle$$

Where $\left|\psi_{12}\right\rangle \in H_A \otimes H_B = H_{AB}$ and the state $\left|\psi_{12}\right\rangle$ is called a separable state because it can be factored into its two component states. This occurs when the Hamiltonian of the two particle system acts on each particle independently, so it can also be factored $\hat{H} = \hat{H}_A \otimes \hat{H}_B$. However, if the Hamiltonian is not factorizable, then the evolution of $|1\rangle$ may depend on $|2\rangle$ and vice versa. This means that the state of the system $\left|\psi_{12}\right\rangle$ may no longer factor into the two states. This is called entanglement.[8]

There are different types of entanglement such as polarization, orbital angular momentum, position, and momentum[12]. In this experiment, momentum-position entangled

particles are used. EPR originally proposed the idealized entangled state

$$\left|\psi_{EPR}\right\rangle = \int_{\infty}^{\infty} |x, x\rangle \, dx = \int_{\infty}^{\infty} \left|p, -p\right\rangle \, dp \tag{1}$$

Here the particles positions are perfectly correlated and their momenta are perfectly anti-correlated. Experimentally, the correlations cannot be perfect, but EPR states can be approximated under suitable conditions[2]. The entanglement correlations mean that actions performed on one particle affect the other particle. At the heart of entanglement, and this experiment, is what Einstein called 'spooky action at a distance', because the entangled particles somehow affect each other even when separated by large distances[8].

2.2 Spontaneous Parametric Down Conversion

Spontaneous Parametric Down Conversion (SPDC) is the method that is used in this experiment to produce position-momentum entangled photons. When light passes through a dielectric material, the electromagnetic wave induces a polarization in the material. This polarization, in turn, affects the wave's subsequent propagation. Usually the relation between the electric field and the polarization vectors is considered to be linear

$$\vec{P}^{(1)} = \epsilon_0 \chi^{(1)} \vec{E} \tag{2}$$

where $\vec{P}^{(1)}$ is the linear polarization field and $\vec{E}$ is the incident electric field. χ is the electric susceptibility. The real component of $\chi^{(1)}$ is related to the index of refraction and the imaginary component is related to the absorption coefficient. According to the above equation, $\chi^{(1)}$ contains all necessary information needed to describe how light interacts with and propagates in a material.[7]

In the field of nonlinear optics, the relationship between the electric field and the polarization can no longer be modelled linearly. Instead the polarization is related to various powers of the electric field by different rank tensors

$$P_i = \epsilon_0(\chi^{(1)}_{ij} E_j + \chi^{(2)}_{ijk} E_j E_k + \chi^{(3)}_{ijkl} E_i E_j E_k + ...) \tag{3}$$

Einstein notation is used, so there is implied summation over repeated indices. $\chi^{(2)}$ is a rank three tensor referred to as the second order nonlinear susceptibility [4]

SPDC is a second-order nonlinear process, which means that it is mathematically modeled by the second order nonlinear susceptibility tensor. SPDC occurs in birefringent materials. In this process, an incident photon (pump photon) instantaneously splits into two lower energy photons (signal and idler). To obey conservation laws, the energy and momenta of the signal and idler photons must sum to that of the pump photon[4] [7]. The signal and idler photons produced are entangled. The creation of the biphoton wavefunction is described mathematically below, following thw work done in [4][15][16].

Materials do not respond to electric fields instantaneously, so equations (2) and (3) are not accurate enough for a rigorous treatment of SPDC. Instead, χ must be a time dependent response function and we must consider previous values of the electric field. In the linear case

$$P(\vec{r},t) = \epsilon_0 \int_0^\infty \chi_{ij}^{(1)}(t') E_j(\vec{r}, t-t')\, dt' \tag{4}$$

and in the second order nonlinear case

$$P_i(\vec{r},t) = \epsilon_0 \int_0^\infty dt' \chi_{ij}^{(1)}(t') E_j(\vec{r},t-t') + \int_0^\infty dt' \int_0^\infty dt'' \chi_{ijk}^{(2)}(t',t'') E_j(\vec{r},t-t') E_k(\vec{r},t-t'') \tag{5}$$

We now define the energy in the field when inside the dielectric.[14]

$$U_E(t) = \frac{1}{2}\int_V d^3\vec{r}(\vec{D}(\vec{r},t)\cdot\vec{E}(\vec{r},t) + \vec{H}(\vec{r},t)\cdot\vec{B}(\vec{r},t)) \tag{6}$$

Where $\vec{H}(\vec{r},t)$ is the magnetic induction and $\vec{B}$ is the magnetic field. We assume that the material is non-magnetic, thus we will not concern ourselves with this term. Then

$$\begin{aligned} U_E &= \frac{1}{2}\int_V d^3\vec{r}(\epsilon_0(1+\chi)\vec{E}\cdot\vec{E} + \vec{B}\cdot\vec{B}) && (7)\\ &= \frac{1}{2}\int_V d^3 r(\epsilon_0\vec{E}\cdot\vec{E} + \vec{B}\cdot\vec{B}) + \frac{1}{2}\int_V d^3 r\epsilon_0\chi\vec{E}\cdot\vec{E} && (8)\\ &= \frac{1}{2}\int_V d^3 r(\epsilon_0(1+\chi^{(1)})\vec{E}\cdot\vec{E} + \vec{B}\cdot\vec{B}) + \frac{1}{2}\int_V d^3 r\epsilon_0\chi_{NL}\vec{E}\cdot\vec{E} && (9)\\ &= U_0 + U_1 && (10) \end{aligned}$$

Where the U_0 term is the linear interaction and the U_1 deals with the nonlinear part, so we focus on U_1 for analyzing SPDC. Disregarding U_0 means we are only considering the cases where SPDC occurs and ignoring the cases where the pump beam passes through the media

unaffected by nonlinear effects. U_1 can be expressed as

$$U_1 = \frac{1}{2}\int d^3r\vec{E}\cdot\vec{P}_{nl} \tag{11}$$

$$= \frac{1}{2}\int_V d^3r\epsilon_0\int_0^\infty dt'\int_0^\infty dt''\chi^{(2)}_{ijk}(t',t'')E_i(\vec{r},t)E_j(\vec{r},t-t')E_k(\vec{r},t-t'') \tag{12}$$

The above equation considers three different electric fields. In the context of SPDC these are the pump, signal, and idler fields, and the subscripts become p,s,i to reflect this.
For this treatment of SPDC we must use the quantized electric field[15].

$$\hat{E}(\vec{r},t) = \frac{i}{c}\sum_{k,n}\omega_k\frac{c\sqrt{2\pi h}}{\omega_k V}(\hat{a}_{k,n}e^{i(\vec{k}\cdot\vec{r}-\omega_k t)} + \hat{a^\dagger}_{k,n}e^{-i(\vec{k}\cdot\vec{r}-\omega_k t)}) \tag{13}$$

Each field, $\vec{E}_m$, can be broken up.

$$\vec{E}_m(\vec{r},t) = \vec{E}^+_m(\vec{r},t) + \vec{E}^-_m(\vec{r},t) \tag{14}$$

Considering the equation for the quantized electric field, the nonlinear Hamiltonian, U_1, will contain eight terms. Each term corresponds to a different, independent second order nonlinear process. Fortunately, we can neglect all of these except for SPDC because our initial conditions include only a single input field. The only energy conserving contributions are where pump photons are annihilated, and signal-idler photon pairs are created, and the reverse process[15][16].

$$\hat{H} = \frac{\epsilon_0}{2}\int_V d^3\vec{r}\chi^{(2)}_{eOO}E^{e,+}_p\hat{E}^{O,-}_s E^{O,-}_i + H.C. \tag{15}$$

Where H.C., the Hermitian Conjugate, represents the case where the signal and idler interact to create a pump photon. This scenario can also be neglected because the signal and idler fields are very weak and $\chi^{(2)}$ is already very small. The power of the signal and idler is not enough to produce such nonlinear effects[15][16]. Therefore:

$$\hat{H} = \frac{\epsilon_0}{2}\int_V d^3\vec{r}\chi^{(2)}_{eOO}E^{e,+}_p\hat{E}^{O,-}_s\hat{E}^{O,-}_i \tag{16}$$

In the above equation the pump field is not an operator because the pump has so many photons that it can be treated classically. The e,O,O scripts indicate extraordinary and ordinary polarization. Since we are using a negative uniaxial BBO crystal, we will only see an extraordinarily polarized pump photon convert into two ordinarily polarized photons. This

is called Type 1 SPDC[19]

The nonlinear susceptibility term is made up of three terms, but the latter two are negligible.

$$\chi^{(2)}_{eoo}(\omega_p,\omega_s,\omega_i) = \chi^{(2)}_{eoo}(\omega_p = \omega_s+\omega_i) + \chi^{(2)}_{eoo}(\omega_i = \omega_s+\omega_p) + \chi^{(2)}_{eoo}(\omega_s = \omega_p+\omega_i) \tag{17}$$

To observe the behavior of this system in time, we apply the evolution operator to the vacuum:

$$\left|\psi(t)\right\rangle = \hat{U}(t)\left|0\right\rangle \tag{18}$$

where

$$\hat{U}(t) = exp[\frac{-i}{\hbar}\int_0^t d\tau \hat{H}(\tau))] \approx 1 + \frac{-i}{\hbar}\int_0^t d\tau \hat{H}(\tau) \tag{19}$$

Substituting in our Hamiltonian, the wavefunction is[15]

$$\begin{aligned}\left|\psi(t)\right\rangle = |0\rangle + \frac{-i}{\hbar}\int_0^t d\tau \chi^{(2)}_{eoo}(\frac{\epsilon_0}{2})... \\ \int_V d^3\vec{r}\int d^3\vec{k}_p\int d^3\vec{k}_s\int d^3\vec{k}_i\{E^e_{op}(\vec{k}_p)U_E(\omega_s)U_E(\omega_i)\hat{a}^\dagger_s(\omega_s,\vec{k}_s,0)\hat{a}^\dagger_i(\omega_i,\vec{k}_i,0)... \\ \times exp(i(\vec{k}_p-\vec{k}_s-\vec{k}_i)\cdot\vec{r}\cdot -i(\omega_p-\omega_s-\omega_i)\tau)\left|0\right\rangle\}\end{aligned} \tag{20}$$

First, let's tackle the time integral:

$$\begin{aligned}\left|\psi(t)\right\rangle = \frac{-i}{\hbar}\chi^{(2)}_{eoo}\frac{\epsilon_0}{2}... \\ \int_V d^3\vec{r}\int d^3\vec{k}_p\int d^3\vec{k}_s\int d^3\vec{k}_i\{E^e_{op}(\vec{k}_p)U_E(\omega_s)U_E(\omega_i)\hat{a}^\dagger_s(\omega_s,\vec{k}_s,0)\hat{a}^\dagger_i(\omega_i,\vec{k}_i,0)... \\ exp(i(\vec{k}_p-\vec{k}_s-\vec{k}_i)\cdot\vec{r})\times exp(-i(\omega_p-\omega_s-\omega_i)\frac{t}{2})\,\mathrm{sinc}(\frac{t}{2}(\omega_s+\omega_i-\omega_p))\left|0\right\rangle\}\end{aligned} \tag{21}$$

And now resolve the volume integral:

$$\begin{aligned}\left|\psi(t)\right\rangle = \frac{-i}{\hbar}\chi^{(2)}_{eoo}\frac{\epsilon_0}{2}... \\ \int d^3\vec{k}_p \int d^3\vec{k}_s \int d^3\vec{k}_i \{E^e_{op}(\vec{k}_p)U_E(\omega_s)U_E(\omega_i)\hat{a}^\dagger_s(\omega_s,\vec{k}_s,0)\hat{a}^\dagger_i(\omega_i,\vec{k}_i,0)... \\ exp(i(\omega_s+\omega_i-\omega_p)\frac{t}{2})\,\mathrm{sinc}(\frac{t}{2}(\omega_s+\omega_i-\omega_p))\prod_m \mathrm{sinc}(\frac{l_m}{2}(\vec{k}_s+\vec{k}_i-\vec{k}_p))exp(-i(\vec{k}_s+\vec{k}_i-\vec{k}_p)_m\frac{l_m}{2})\left|0\right\rangle\}\end{aligned} \tag{22}$$

Here we make a couple approximations[15][16]:

- The transverse crystal dimensions are large compared to the transverse cross section of the pump, mathematically:

$$\mathrm{sinc}((\vec{q}_s+\vec{q}_i-\vec{q}_p)\frac{\vec{l}_T}{2}) = \delta(\vec{q}_s+\vec{q}_i-\vec{q}_p)$$

  Where $\vec{q}$ is the transverse component of the wavevector.

- $dk_z = dk$ and $k_z \approx k(1-\frac{|q|^2}{2k^2})$ maximal approximation
- t is large enough so that $\mathrm{sinc}((\omega_s+\omega_i-\omega_p)\frac{t}{2} \approx \delta(\omega_p-\omega_s-\omega_i)$
- the pump is approximately monochromatic: $E^e_{op}(\vec{k}_p) = \nu(\vec{q}_p)\delta(\omega_p-k_0)$

Then, in steps

$$\begin{aligned}\left|\psi(t)\right\rangle = \\ \frac{-i}{\hbar}\chi^{(2)}_{eoo}\frac{\epsilon_0}{2}\int d^3\vec{k}_p\int d^3\vec{k}_s\int d^3\vec{k}_i\nu(\vec{q}_p)\delta(k_p-k_s)U_E(\omega_s)U_E(\omega_i)... \\ \hat{a}^\dagger_s(\omega_s,\vec{k}_s,0)\hat{a}^\dagger_i(\omega_i,\vec{k}_i,0)\delta(\omega_p-\omega_s-\omega_i)\delta(\vec{q}_s+\vec{q}_i-\vec{q}_p)... \\ exp(-i(\vec{q}_s+\vec{q}_i-\vec{q}_p)\frac{\vec{l}_T}{2})\,\mathrm{sinc}(\frac{l_z}{2}(\vec{kz}_s+\vec{kz}_i-\vec{kz}_p))exp(-i(\vec{k}_{zs}+\vec{k}_{zi}-\vec{k}_{zp})\frac{\vec{l}_z}{2})\left|0\right\rangle \\ = \frac{-i}{\hbar}\chi^{(2)}_{eoo}\frac{\epsilon_0}{2}\int d\vec{q}_s\int d\vec{q}_i\int dk_s\int dk_i\int dk_p\nu(\vec{q}_s+\vec{q}_i)U_E(\omega_s)U_E(\omega_i)... \\ \delta(\omega_p-\omega_s-\omega_i)exp(i(\omega_s+\omega_i-\omega_p)\frac{t}{2})\delta(k_p-k_s)\,\mathrm{sinc}\big[\frac{l_z}{2}(k_s+k_i-\frac{|q_s|^2}{2k_s}-\frac{|q_i|^2}{2k_i}+\frac{|\vec{q}_s+\vec{q}_i|^2}{2k_0})\big]... \\ exp(-i(k_s+k_i-k_p-\frac{|q_s|^2}{2k_s}-\frac{|q_i|^2}{2k_i}+\frac{|\vec{q}_s+\vec{q}_i|^2}{2k_0})\frac{l_z}{2})\left|\vec{q}_s,k_s,0\right\rangle\left|\vec{q}_i,k_i,0\right\rangle\end{aligned} \tag{23}$$

If the crystal is thin enough, $\Delta k = 0$, we operate under this assumption:

$$\begin{aligned}\left|\psi(t)\right\rangle = \frac{-i}{\hbar}\chi^{(2)}_{eoo}\frac{\epsilon_0}{2}\int d\vec{q}_s d\vec{q}_i dk_s dk_i v(\vec{q}_s+\vec{q}_i)U_E(\omega_s)U_E(\omega_i)...\\ \text{sinc}[(\Delta k - \frac{|q_s|^2}{2k_s} - \frac{|q_i|^2}{2k_i} + \frac{|\vec{q}_s+\vec{q}_i|^2}{2k_0})\frac{l_z}{2}]\,\text{sinc}(\frac{t}{2}(\omega_s+\omega_i-\omega_0))exp(-i(\omega_s+\omega_i-\omega_0)\frac{t}{2})...\\ exp[-i(\Delta k - \frac{|q_s|^2}{2k_s} - \frac{|q_i|^2}{2k_i} + \frac{|\vec{q}_s+\vec{q}_i|^2}{2k_0})\frac{l_z}{2}]\left|\vec{q}_s,k_s,0\right\rangle\left|\vec{q}_i,k_i,0\right\rangle \quad (24)\end{aligned}$$

Now, the amplitude for coincident detection is given by the destruction (detection) of the signal and idler photons.

$$A(\vec{p}_s,\vec{p}_i) = \langle 0|\,\hat{E}^{(+)}_{s,o}(\vec{p}_s)\hat{E}^{(+)}_{i,o}(\vec{p}_i)\left|\psi(t)\right\rangle \quad (25)$$

Where:

$$\hat{E}^{(+)}_{i,o}(\vec{p}_i) = \int d\vec{q}'_i U_E(k'_j)H_j(\vec{q}'_j)\hat{a}(\vec{q}'_j,k'_j,0)exp(i(\vec{q}'_j\cdot\vec{p}_j - k'_j T)) \quad (26)$$

In the above expression $k'_j = \omega_0 - \omega_k$ and $H-j(\vec{q}'_j) = exp(i\phi(\vec{q}'_j)$. Note that we require detection at time T. Also $k = nk_0 = n\omega/c$. We also assume dispersion is negligible. We get:

$$\begin{aligned}A(\vec{p}_s,\vec{p}_i) = \frac{-i}{\hbar}\chi^{(2)}_{eoo}\frac{\epsilon_0}{2}\int dq'_s dq'_i dq_s dq_i dk_s dk_i v(\vec{q}_s+\vec{q}_i)U_E(k'_s)U_E(k'_i)H_s(\vec{q}'_s)H_i(\vec{q}'_i)...\\ exp(i(\vec{q}'_s\cdot\vec{p}_s + \vec{q}'_i\cdot\vec{p}_i - \omega'_s T - \omega_i T))\times U_E(k_s)U_E(k_i)...\\ \text{sinc}[(-\frac{|q_s|^2}{2k_s} - \frac{|q_i|^2}{2k_i} + \frac{|\vec{q}_s+\vec{q}_i|^2}{2k_0})\frac{l_z}{2}]exp(-i(-\frac{|q_s|^2}{2k_s} - \frac{|q_i|^2}{2k_i} + \frac{|\vec{q}_s+\vec{q}_i|^2}{2k_0})\frac{l_z}{2})\times...\\ exp(-i(\omega_s+\omega_i-\omega_0)\frac{t}{2})\,\text{sinc}[\frac{t}{2}(\omega_s+\omega_i-\omega_o)]\left\langle\vec{q}'_s,k'_s,0\middle|\vec{q}_s,k_s,0\right\rangle\left\langle\vec{q}'_i,k'_i,0\middle|\vec{q}_i,k_i,0\right\rangle\end{aligned} \quad (27)$$

The brakets can be replaced by dirac delta functions and the above equation can be written:

$$A(\vec{p}_s,\vec{p}_i)=\frac{-i}{\hbar}\chi^{(2)}_{eoo}\frac{\epsilon_0}{2}\int d\vec{q}_s d\vec{q}_i U_E^2(k'_s)U_E^2(k'_i)H_s(\vec{q}_s)H_i(\vec{q}_i\times\nu(\vec{q}_s+\vec{q}_i\times\ldots$$
$$exp(i(\vec{q}_s\cdot\vec{p}_s+\vec{q}_i\cdot\vec{p}_i))exp(-i(\omega'_s+\omega'_i)T)\,\mathrm{sinc}[\frac{l_z}{2}(-\frac{|q_i|^2}{2k'_i}-\frac{|q_s|^2}{2k'_s}+\frac{|\vec{q}_s+\vec{q}_i|^2}{2k_0})]\ldots$$
$$exp(-i\frac{l_z}{2}(-\frac{|q_i|^2}{2k'_i}-\frac{|q_s|^2}{2k'_s}+\frac{|\vec{q}_s+\vec{q}_i|^2}{2k_0}))exp(-i((\omega'_s+\omega'_i)-\omega_0)\frac{t}{2})\,\mathrm{sinc}[\frac{t}{2}((\omega'_s+\omega'_i)-\omega_0)] \quad (28)$$

The δ function in k_s and k_i and k'_s and k'_i means that we have chosen k'_s and k'_i since we do not integrate along k'_s and k'_i. This is typically done by choosing narrowband spectral filters at the detection stage. These filters aren't necessarily infintesmally narrow, but for our purposes this approximation is sufficient we will choose the filters such that $k'_s+k'_i=k_0$ and $\omega'_s+\omega'_i=\omega_0$.

Then

$$A(\vec{p}_s,\vec{p}_i)=\frac{-i}{\hbar}\chi^{(2)}_{eoo}\frac{\epsilon_0}{2}\int d\vec{q}_s d\vec{q}_i U_E^2(k_s)U_E^2(k_i)H_s(\vec{q}_s)H_i(\vec{q}_i\times\nu(\vec{q}_s+\vec{q}_i\times\ldots$$
$$exp(-i\frac{l_z}{2}(-\frac{|q_i|^2}{2k'_i}-\frac{|q_s|^2}{2k'_s}+\frac{|\vec{q}_s+\vec{q}_i|^2}{2k_0}))\,\mathrm{sinc}[\frac{l_z}{2}(-\frac{|q_i|^2}{2k'_i}-\frac{|q_s|^2}{2k'_s}+\frac{|\vec{q}_s+\vec{q}_i|^2}{2k_0})]\ldots$$
$$exp(-i\omega_0 T)exp(i(\vec{q}_s\cdot\vec{p}_s+\vec{q}_i\cdot\vec{p}_i)) \quad (29)$$

This is the probability amplitude in the position representation. In the momentum representation the amplitude is:

$$\tilde{A}(\vec{p}_s,\vec{p}_i)=\frac{-i}{\hbar}\chi^{(2)}_{eoo}\frac{\epsilon_0}{2}U_E^2(k_s)U_E^2(k_i)H_s(\vec{q}_s)H_i(\vec{q}_i\times\nu(\vec{q}_s+\vec{q}_i\times exp(-i\frac{l_z}{2}(-\frac{|q_i|^2}{2k'_i}-\frac{|q_s|^2}{2k'_s}+\frac{|\vec{q}_s+\vec{q}_i|^2}{2k_0}))\ldots$$
$$\mathrm{sinc}[\frac{l_z}{2}(-\frac{|q_i|^2}{2k'_i}-\frac{|q_s|^2}{2k'_s}+\frac{|\vec{q}_s+\vec{q}_i|^2}{2k_0})]exp(-i\omega_0 T) \quad (30)$$

2.3 Ghost Imaging

In classical imaging, the photons that create the image are the same photons that interacted with the object, just modified by the lens system's transfer function. Ghost imaging also has a point-to-point image-forming relationship between the object and image planes, but it differs from classical imaging because the photons incident on the image plane do not

"come" from the object plane. Ghost imaging techniques use pairs of photons. One photon in the pair interacts with the object and the other one hits the imaging plane. The information of the object must be transferred somehow using correlations between the photons. These correlations can be created through either classical or quantum means [13]. In our experiment the correlations are due to quantum entanglement.

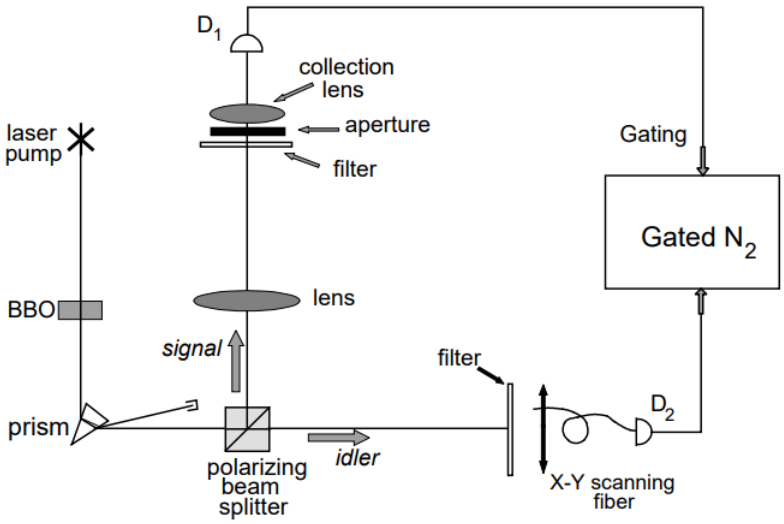

Figure 1: A diagram of the first ghost imaging experiment done in 1995. The object in this diagram is the 'aperture'. [17]

The process of quantum ghost imaging uses the position correlations between the signal and idler photons created in SPDC. After disposing of the pump beam, the signal and idler photons are sent along different paths. The signal photon illuminates an object/mask. Behind the object is a bucket detector such as an avalanche photodiode (APD) that is kept in a fixed position. The idler photon hits an optical detector that has spatial resolution. The output of the detectors is used for coincidence counting to detect signal-idler pairs. Due to the position entanglement, the position of the detected idler photon reveals the position of the signal photon, detected or not. Therefore, through the coincidence counts, the mask is 'imaged' by the idler photon on the detector with resolution, even though this photon never interacted with the object[5].

2.4 Previous Work

Non-local aberration cancellation has already been experimentally realized by Nick Black in 2019[3]. The aberration cancellation in his experiment produced successful results, as shown in Fig. 2.

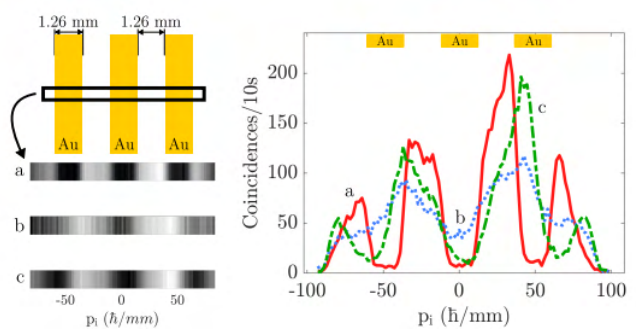

Figure 2: Results of the 2019 aberration cancellation experiment. Three gold bars were imaged in one dimension. First a) they were imaged with no aberrations (red line), then b) with defocus introduced (blue line), then c) with the defocus cancelled out (green line). Image is almost completely restored.

The purpose of the current experiment is to reconstruct the 2019 experiment, but with the important change that this experiment uses signal and idler photons of different wavelengths. In this experiment the signal photon, incident on the bucket detector, will be in the infrared and the idler photon will be visible. This is important because it shows potential for applications in IR imaging. IR imaging is difficult with current technology because high resolution IR cameras are expensive. Two color aberration ghost imaging and aberration cancellation will demonstrate that it is possible to image in the infrared, and then correct for aberrations and detect in the visible regime.

3 EXPERIMENTAL SETUP

Our setup includes a CW laser source, a nonlinear periodically poled potassium titanyl phosphate (PPKPT) crystal, a spatial light modulator (SLM), a deformable mirror, a bucket detector, and a CCD detector. The roles and specifics of these components will be discussed in this section. Our setup also involves numerous minor optical components such as waveplates, lenses, and flat mirrors. These will not be discussed in depth.

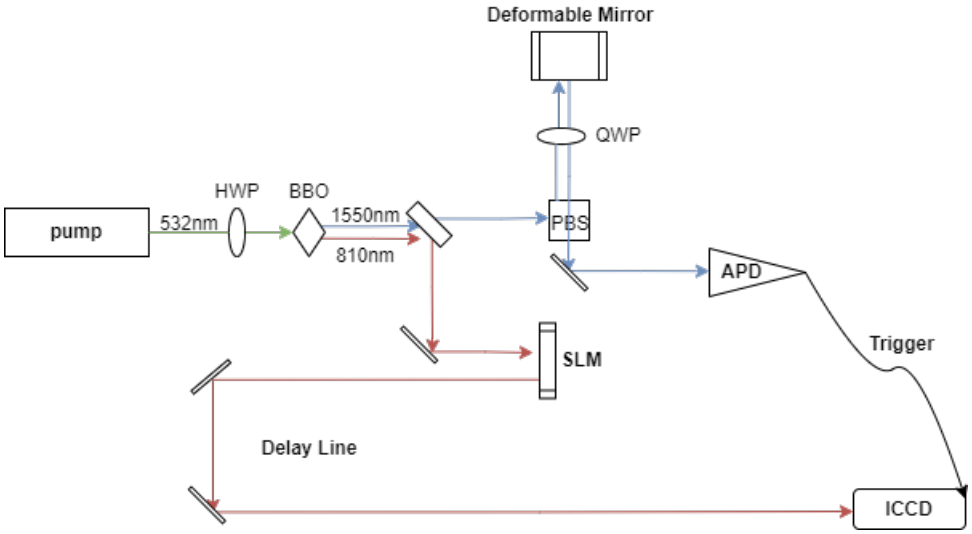

Figure 3: A diagram of the final setup needed for aberration cancellation

3.1 Laser Source

Our laser source is a Spectra-Physics Millennia Vs. It is a 532nm second harmonic generation CW laser. It has variable power that can be increased up to 5W, but for our purposes we only need 100mW.

3.2 Nonlinear Crystal

We began with a periodically poled potassium titanyl phosphate (PPKTP) crystal for SPDC. The company that we purchased the crystal from could not provide us with the optimum temperature to heat the crystal to to maximize SPDC. In late February we switched out this crystal for a beta barium borate (BBO) crystal. The BBO crystal does not need to be heated. The BBO crystal is also superior because it is thinner along the optical axis. This improves the co-linearity of our signal and idler photons.

SPDC is governed by the phase matching condition. In collinear SPDC, the condition $\Delta k_z = 0$ makes the phase matching equation

$$n_{p\sigma}(\omega_{p0}) - n_{s\sigma}(\omega_{s0}) = \frac{\omega_{i0}}{\omega_{p0}}(n_{i\sigma}(\omega_{i0}) - n_{s\sigma}(\omega_{s0})) \tag{31}$$

where $\sigma = o, e$ can represent ordinary or extraordinary axis polarization. Our BBO crystal is Type-I. It is a negative uniaxial crystal, meaning $n_o > n_e$. Noting this, and also noting that

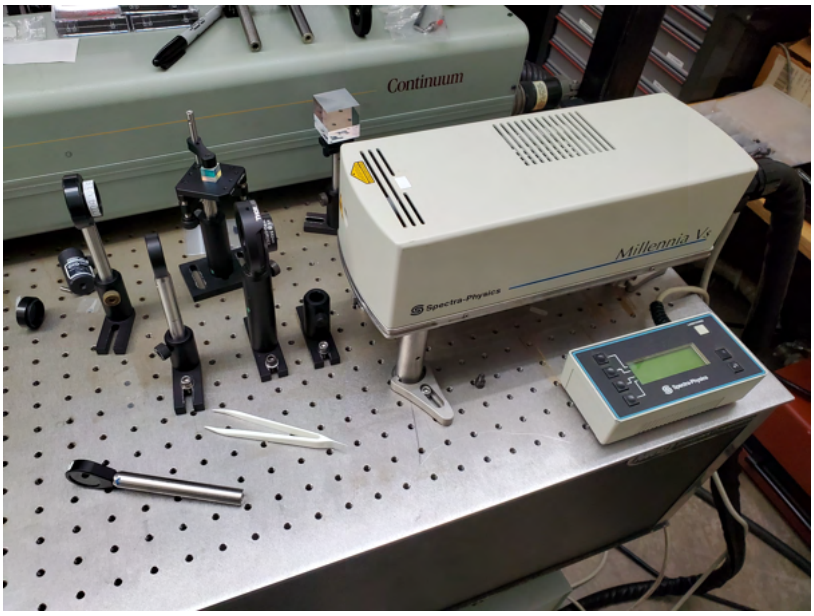

Figure 4: A picture of our laser source. In front of the laser is a half waveplate and a neutral density filter.

$\omega_{s0} \geq \omega_{p0}$, equation (31) holds true when the pump is polarized along the extraordinary axis and the signal and idler are along the ordinary axis. This is usually written as $e \rightarrow o + o$.[19] This is important because it provides us a way to check that our detected photons are actually downconverted photons. We can change the pump polarization, and if the detected counts change, then they are from SPDC.

3.3 Spatial Light Modulator

Our spatial light modulator (SLM) is a Santec SLM-200. An SLM is a device with a 2D aperture that can be manipulated to precisely modulate the phase of incident light. Our model uses a liquid crystal on silicon (LCOS) aperture which gives it 1024 gray levels, HD resolution, and phase stability of 0.001π rad[9].

3.4 Deformable Mirror

Our deformable mirror is from Boston Micromachines. It has a similar function to an SLM, except that its reflective surface is modified by sixteen tiny actuators behind the mirror. This allows the mirror to take whatever shape the user desires.

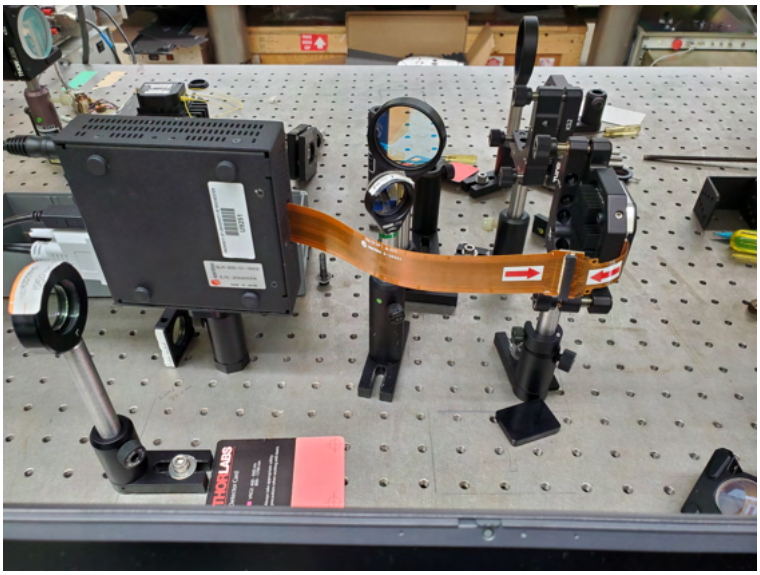

Figure 5: The SLM consists of a control box that must be carefully connected to the LCOS aperture mounted on a post.

3.5 The Delay Line

The delay line runs from the SLM to the ICCD. It consists of several $4f$ imaging systems, and one lens system that magnifies the beam by $M \approx 2x$ onto the ICCD. The purpose of the delay line is to give the ICCD time to trigger. The 1550nm signal photon hits the APD. It takes time for the APD to register it, and then send the signal to the ICCD to trigger. If the idler photon arrives at the ICCD before the trigger signal does, we will not be able to capture it with the ICCD. Therefore, in planning this setup, we made rough estimates of how much delay we needed, and where we should see coincidence counts. First, we estimated the time it takes for the idler photon to be detected by the APD and sent to trigger the ICCD:

Free space propagation	2ns
Multimode fiber to APD	5ns
APD internal delay	4ns
Coaxial cable to ICCD	5ns
Total	16ns

The delay line we constructed was approximately 27m long. This corresponds to 90ns of signal photon travel. Therefore, we expect to see coincidences at approximately 74ns. The ICCD camera takes a minimum of 27ns to trigger, so 74ns gives us 47ns of leeway.

3.6 Detectors

Our CCD detector is a Princeton Instruments PI-MAX 4 ICCD. This camera has <500 psec gating time, which is useful for our purposes because we need to time our camera triggering correctly. The small gating time is negligible in our triggering and delay line calculations.[10]. We put a narrow bandpass filter in front of the camera to ensure that only 810nm light is able to hit the detector.

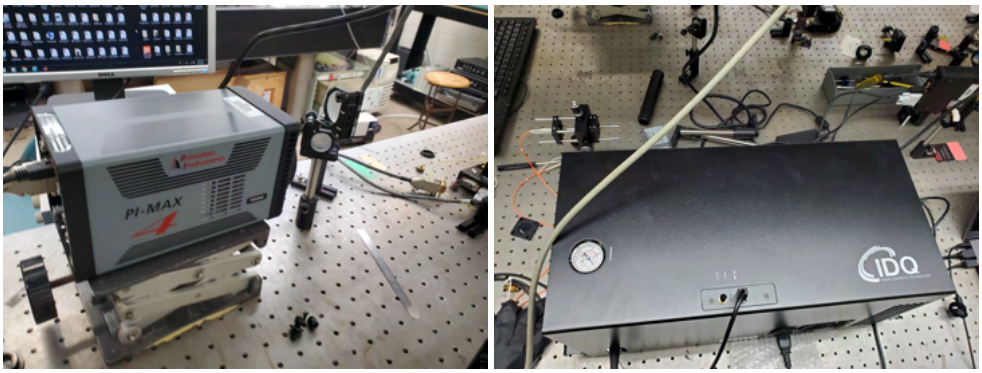

Figure 6: (left) The ICCD detector. (right) The infrared detector.

Our second detector, the bucket detector, is an IDQ ID230 Infrared Single-Photon Detector. This is an avalanche photodiode.This detector has 150ps timing resolution, which is very useful because it is also small enough that it doesn't disrupt the trigger delay timing. The photons are actually incident on a multimode fiber with an aperature, and the fiber is then connected to this detector. A 1550nm narrow band-pass filter was put on this detector.

4 PRELIMINARY RESULTS

4.1 SLM Calibration

The SLM needed to be calibrated so that we know the relationship between changes in grey value and changes in phase. To do this, a polarizer was inserted after the SLM, and it was rotated so that counts were approximately minimized at grey value of zero. Then the SLM ran through its grey values, 0 to 1023, and we recorded the counts (proportional to power) on the detector every 10 grey values.

In figure 6 the normalized counts are plotted as a function of the grey value. Due to Malus

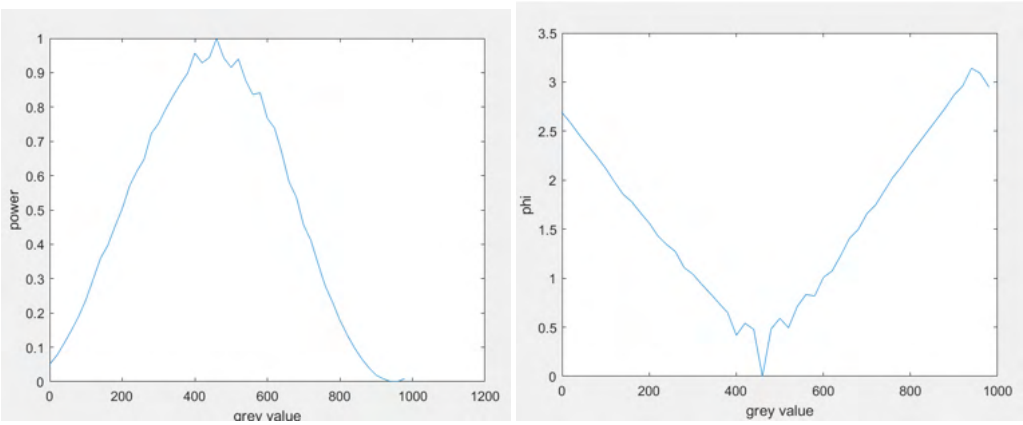

Figure 7: SLM calibration data.

Law, this is a $\cos^2$ function. Using the formula

$$\phi = \cos^{-1}(2P-1) \tag{32}$$

Where P is the normalized power, we can get ϕ as a function of the grey value. In the middle of this plot it sharply changes direction because of the modular nature of inverse cosine. Unravelling this and making a linear fit gives a slope of 2.6, which is used to relate grey value to phase.

4.2 Obtaining Focused Image on Detector

Our system was setup to image the crystal's plane onto the detector. To check for a sharp image we put a mask on the crystal. The camera did not have a fine z-axis adjustment, so instead a quadratic phase was added on the SLM to correct for the defocus. The best focused image was verified by eye. Fig. 8 shows the focused mask on the crystal.

5 PROBLEMS AND PROGRESS

5.1 Ghost Image Attempt

With a good image on the camera, obtaining ghost imaging was the next goal. A ghost image verifies both the triggering of the ICCD and the spatial correlations of the entangled photons. To set the system up for ghost imaging, the APD is connected to a coincidence counting unit (CCU). Rather than counting coincidences, this is just used to count the number of photons incident on the detector per second.

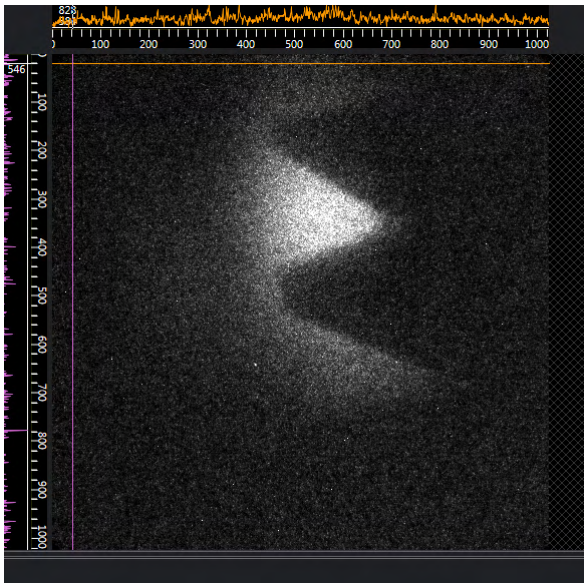

Figure 8: In focus image of the crystal with a zig-zag mask.

First we tuned the APD's position to maximize counts. We were able to achieve $S/N \approx 10$, which is adequate for this experiment. A mask was inserted in front of the APD. We verified that the counts were approximately halved, meaning the mask was partially blocking the signal as intended. Then the coaxial cable was disconnected from the CCU and connected to the ICCD camera input trigger port. Many different settings were varied on the ICCD, but no ghost image was obtained.

We double-checked everything we had done, including realigning the system, refocusing the camera, and realigning the APD. Still no ghost image could be found. After much troubleshooting, we found several possible issues:

Modifying the polarization of the pump beam revealed that stray light was incident on the ICCD (see section 3.2), so we took the 1550nm narrow band-pass filter from in front of the ICCD and tested it using an Ocean Optics spectrometer. Looking at the spectrometer data, it was obvious that this filter was out of spec. and was hindering our experiment. The filter was returned to the supplier and a different filter was inserted.
We also discovered that we were losing a significant amount of light at the dichroic mirror that splits the signal and idler beams. The mirror was in a mount that limited its aperture to a point that it was over-filled by the beam. The mirror was remounted, which also required re-alignment of the system.
Even after replacing the 1550nm filter, the counts on the APD were still coming from some-

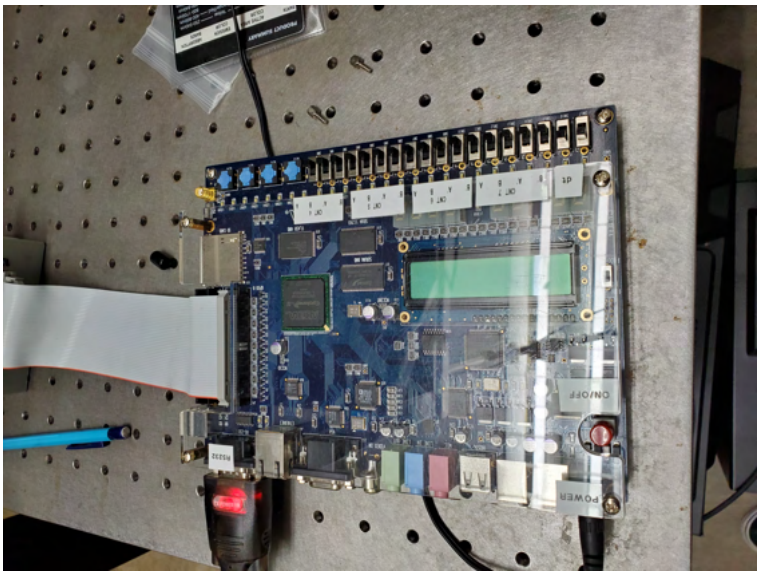

Figure 9: Our CCU uses Dr. Mark Beck's [18] program on an Altera De2 FPGA.

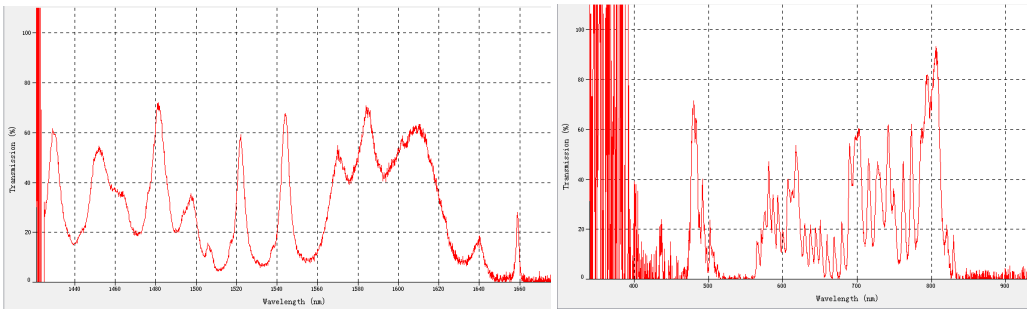

Figure 10: Spectrometer data showing that our 1550nm narrow band-pass filter isn't much of a filter.

thing other than the entangled photons. Some unwanted light was somehow triggering the APD. We found that scattered light was going around the 1550nm filter and objective, through the cage mount, and incident on our APD fiber. To remedy this, a makeshift cover was made to protect this area from scattered light, and APD counts were then verified to be from SPDC with $SNR \approx 13$

6 End of Semester Results

6.1 Coincidence Counts

After two failed attempts at ghost imaging, we reset our goal to the intermediate result of obtaining coincidence counts. To look for coincidence counts, we moved the APD fiber closer

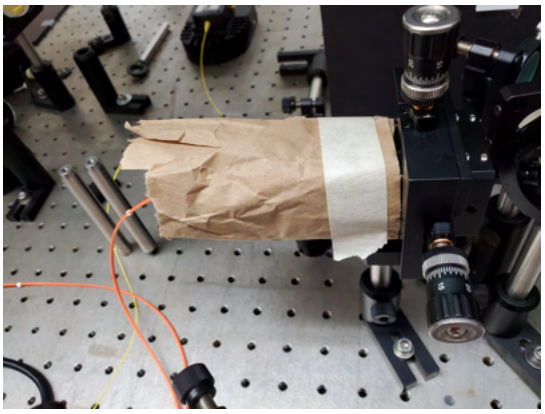

Figure 11: The cage mount housing our APD's fiber, objective, and 1550nm filter. The makeshift shield prevented stray light.

to the crystal. This made it so that the crystal wasn't imaged onto the detector, meaning ghost imaging wouldn't be possible. However this made it much easier to get high SPDC counts on the APD. Not having to worry about perfectly imaging the crystal also meant that we could be more flexible in moving the ICCD to find the image.

Once counts were maximized on the APD and the beam was centered on the ICCD, the coaxial cable was set up to allow the APD to trigger the ICCD. To verify coincidence counts, there should be a narrow window of only a few nanoseconds in the ICCD's tunable delay that shows incident photons. The ICCD's delay starts at 27ns. A gate width of 10ns was selected and data was taken while varying the delay by 10ns. Photons were noticed on the detector at a delay of 57ns. The delay was narrowed down to 63ns, and the gate width was narrowed down to 5ns. Figure 12 shows captures of the data with delays of 60ns, 63ns, and 65ns. In the 63ns a feint spot can be seen in the middle of the aperture that is not apparent in the 60ns and 65ns shots.

6.2 SLM Matlab Code

For aberration cancellation to work, the SLM needs to have the opposite aberration of the deformable mirror. Theoretically it doesn't matter which device 'creates' and 'cancels' the aberration. Experimentally speaking, however, the defomable mirror creates the aberrations and the SLM cancels them. This is because the deformable mirror's sixteen actuators cannot be as precise as the SLM's 1200x1900 LCOS display. It is best to start with the deformable mirror because we know the SLM will be capable of cancelling any of the deformable mirror's aberrations while the opposite isn't true.

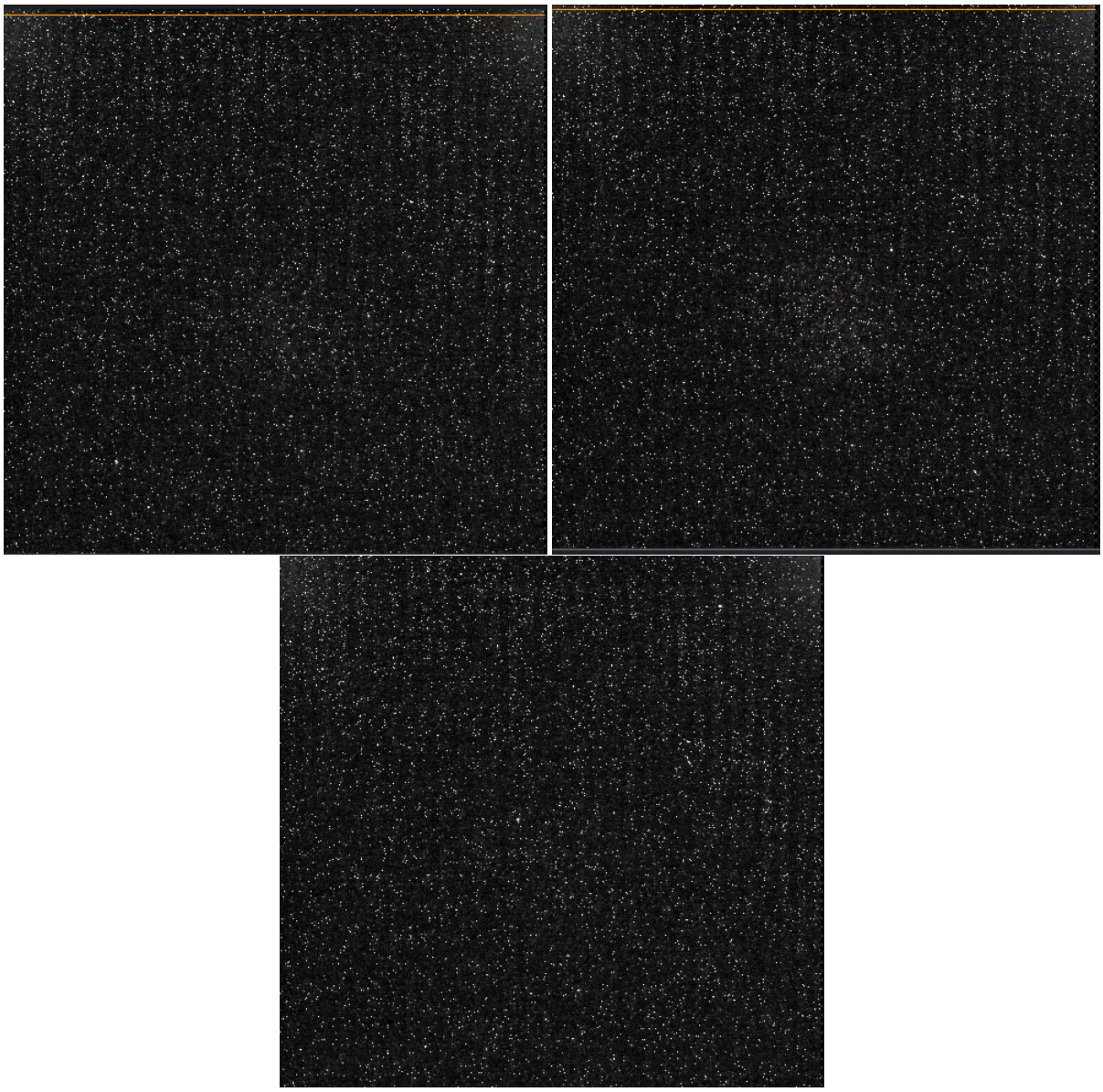

Figure 12: Three ICCD captures. Top Left: 60ns, Top Right: 63ns with feint spot in middle signifying coincidence coutns, Bottom: 65ns

The deformable mirror's simplicity makes it easily controllable with its user friendly software. To put a desired aberration on the SLM, however, requires a csv file specifying the grey value of each pixel. A Matlab code was written to accomplish this.

The Matlab script first creates a 1200x1900 array dependent on the desired aberration. For example, to get defocus the array values scale $\propto \rho^2$. The code then accounts for the SLM's calibration (see Section 4.1), which relates the pixels' grey value to the phase. Lastly, the code then formats this array according to the SLM manual's specifications and outputs to a csv file.

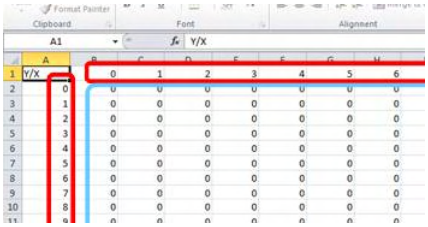

Figure 13: The SLM requires that csv files contain the array with axes and the first entry reading 'X/Y'

7 THE FUTURE OF THE PROJECT

Unfortunately, this project couldn't be completed by the thesis deadline of May 1st, 2022. I intend to keep working on this experiment until May 12th. At that point, a graduate student named Yi Wang will take over the experiment.
Achieving coincidence counts was important because it tells us that everything in the experiment is working properly. Obtaining a ghost image is the next step. This will be accomplished by placing the APD fiber and ICCD so that they are in the image plane of the crystal. Accumulating enough photons to obtain a ghost image will necessitate a long data collection process. After ghost imaging, aberrations should be inserted. Since the code for the SLM is already written and the SLM is already in place, this should be a simple process. I am confident that this project will continue to a successful conclusion.

8 BUDGET

This project is funded by the United States Department of Energy (DOE). We are working in collaboration with the Pacific Northwest National Lab. Resources from Robert Boyd's lab are also used.

9 ACKNOWLEDGEMENTS

I would like to thank Nick Black for sharing this project with me and for taking time to help me better understand it. I would like to thank Prof. Robert Boyd for being my thesis advisor and allowing me to be a research assistant in his group. I would also like to thank Giulia Marcucci for guiding me through the tough theoretical parts of quantum optics. Finally, I would like to thank Garrett Beals and Benjamin Nussbaum for being amazing friends and examples to me during my undergraduate career.

REFERENCES

[1] Schrödinger, E., Born, M. (1935). Discussion of Probability Relations between Separated Systems. Mathematical Proceedings of the Cambridge Philosophical Society, 31(04), 555. doi:10.1017/s0305004100013554

[2] Howell, John C.; Bennink, Ryan S.; Bentley, Sean J.; Boyd, R. W. (2004). Realization of the Einstein-Podolsky-Rosen Paradox Using Momentum- and Position-Entangled Photons from Spontaneous Parametric Down Conversion. Physical Review Letters, 92(21)

[3] A. N. Black, E. Giese, B. Braverman, N. Zollo, and R. W. Boyd, "Quantum, Nonlocal Aberration Cancellation," in Conference on Lasers and Electro-Optics, OSA Technical Digest (Optical Society of America, 2019), paper FF3A.6.

[4] Schneeloch, James. *On Position-Momentum Entanglement, Nonlocality, and Measurement*. 2015. University of Rochester. PhD Dissertation.

[5] Y. Shih, "The physics of ghost imaging," in International Conference on Quantum Information, (Optical Society of America, 2008), paper QTuB1.

[6] Marco Fiorentino, Sean M. Spillane, Raymond G. Beausoleil, Tony D. Roberts, Philip Battle, and Mark W. Munro, "Spontaneous parametric down-conversion in periodically poled KTP waveguides and bulk crystals," Opt. Express 15, 7479-7488 (2007)

[7] Boyd, Robert. *Nonlinear Optics*. 4th Ed. Elievier, 2020. Print.

[8] Scheck, Florian. *Quantum Physics*. 2nd Ed. Springer, 2013. Print.

[9] Santec Corp. *Spatial Light Modulator*.https://www.santec.com/en/products/components/slm/?gclid=CjwKCAiAksyNBhAPEiwAlDBeLLbl9ZwoQ899uBUitRQ7mTrNXCMMPb4bkFD-oqF9kLG7HorlwFKtBoCcoUQAvD_BwE

[10] Princeton Instruments. *PI MAX4*.https://www.princetoninstruments.com/products/pi-max-family/pi-max

[11] ID Quantique. *ID230 Infrared Single Photon Detecor*.https://www.idquantique.com/quantum-sensing/products/id230/?utm_source=google_ads_search&utm_medium=cpc&gclid=CjwKCAiAksyNBhAPEiwAlDBeLO1eGCQF_9EzN8qiddDcVc91-hG4Jxa5doffC-MAQWNfh0Wj4GBtbBoCs_YQAvD_BwE

[12] Paul G. Kwiat (1997) Hyper-entangled states, Journal of Modern Optics, 44:11-12, 2173-2184

[13] Padgett Miles J. and Boyd Robert W. 2017An introduction to ghost imaging: quantum and classicalPhil. Trans. R. Soc. A.3752016023320160233

[14] Mandel, Leonard and Wolf, Emil. *Optical Coherence and Quantum Optics.* New York, Cambridge University Press, 1995. Print.

[15] Black, Nick. "Quantum Optics Crash Course." Lecture, University of Rochester, March 1, 2022.

[16] Walborn, Stephen Monken, Carlos Pádua, S. Souto Ribeiro, Paulo. (2010). Spatial correlations in parametric down-conversion. Physics Reports. 495. 87-139. 10.1016/j.physrep.2010.06.003.

[17] Pittman TB, Shih YH, Strekalov DV, Sergienko AV. Optical imaging by means of two-photon quantum entanglement. Phys Rev A. 1995 Nov;52(5):R3429-R3432. doi: 10.1103/physreva.52.r3429. PMID: 9912767.

[18] `http://people.reed.edu/~beckm/QM/circuit/circuit.html`

[19] Karan, Suman Aarav, Shaurya Bharadhwaj, Homanga Taneja, Lavanya De, Arinjoy Kulkarni, Girish Meher, Nilakantha Jha, Anand. (2018). Phase matching in -barium borate crystals for spontaneous parametric down-conversion.